Short-range charge density wave order in 2H-TaS_{2}

Jaydeep Joshi, Heather M. Hill, Sugata Chowdhury, Christos D. Malliakas, Francesca Tavazza, Utpal Chatterjee, Angela R. Hight Walker, and Patrick M. Vora

Phys. Rev. B **99**, 245144 — Published 25 June 2019

DOI: 10.1103/PhysRevB.99.245144

Short Range Charge Density Wave Order in 2H-TaS_2

Jaydeep Joshi[1,2], Heather M. Hill[3], Sugata Chowdhury[4], Christos D. Malliakas[5], Francesca Tavazza[4], Utpal Chatterjee[6], Angela Hight Walker[3] and Patrick M. Vora [1,2,*]

[1]*Department of Physics and Astronomy, George Mason University, Fairfax, VA USA*
[2]*Quantum Materials Center, George Mason University, Fairfax, VA USA*
[3]*Physical Measurement Laboratory, National Institute of Standards and Technology, Gaithersburg, MD USA*
[4]*Materials Measurement Laboratory, National Institute of Standards and Technology, Gaithersburg, MD USA*
[5]*Department of Chemistry, Northwestern University, Evanston, IL USA*
[6]*Department of Physics, University of Virginia, Charlottesville, VA USA*

Keywords: *Raman spectroscopy, charge density waves, tantalum disulfide, correlated electron physics, density functional theory*

Abstract

2H-TaS_2 undergoes a charge density wave (CDW) transition at $T_{CDW} \sim 75$ K, however key questions regarding the onset of CDW order remain under debate. In this study, we explore the CDW transition through a combination of temperature and excitation-dependent Raman spectroscopy, angle resolved photoemission spectroscopy (ARPES), and density functional theory (DFT). Below T_{CDW} we identify two CDW amplitude modes that redshift and broaden with increasing temperature and one zone-folded mode that disappears above T_{CDW}. Above T_{CDW}, we observe a strong two-phonon mode that softens substantially upon cooling, which suggests the presence of substantial lattice distortions at temperatures as high as 250 K. This correlates with the ARPES observation of the persistence of CDW energy gap above T_{CDW} and finite-temperature DFT calculations of the phonon band structure that indicate an instability occurring well above the CDW transition temperature. DFT also provides the atomic displacements of the CDW amplitude modes and reproduces their temperature-dependence. From these observations we suggest that short range CDW order exists well-above T_{CDW} which poses new questions regarding the interplay between electronic structure and vibrational modes in layered CDW materials.

Introduction

Group V transition metal dichalcogenides (TMDs) belong to a broad class of two-dimensional (2D) materials that exhibit CDWs and superconductivity. CDWs are periodic modulations of the electron densities, accompanied by a simultaneous distortion of the crystal lattice where the relative periodicity is governed by the location of the CDW gap in the Brillouin zone. The CDW phase can be incommensurate, nearly commensurate, or commensurate with the underlying lattice which governs the relative mismatch between lattice periodicity and charge modulation. In 2D and quasi-2D systems, strong electron-phonon interactions at low temperatures drive the CDW transition,[1–4] as opposed to other mechanisms such as Fermi surface nesting[5,6], exciton-phonon interactions[7–9] and saddle-points near Fermi energy (E_F).[10] Moreover, recent observations of opposite trends in layer-dependent CDW and superconducting transition temperatures for 2H-$NbSe_2$[11] and 2H-TaS_2[12–14] have prompted new questions regarding the CDWs in 2D materials. In addition, the electronic phase diagram of layered CDW materials is highly dependent on the polymorph. TaS_2 serves as an ideal example: 1T-TaS_2 exhibits transitions between incommensurate, nearly-commensurate, and commensurate CDW phases whereas 2H-TaS_2 only has a single transition from a conventional metallic phase to an incommensurate CDW phase.[15] The more exotic 3R and 2Hb-TaS_2[16] structural phases reveal additional complexity and illustrate the incredible diversity in the CDW order parameter even with identical chemical composition.

In this study we explore the incommensurate CDW state in bulk 2H-TaS_2 which appears below T_{CDW} ~ 75 K. While prior examinations of this material focused on CDWs with electrical and structural techniques,[12,17–21] only two studies of CDW phonon modes and their associated temperature-dependence have been reported: One performed nearly four decades ago[22] and a second recent work that focused on the superconducting Higgs mode.[23] By combining temperature and excitation-dependent Raman spectroscopy, DFT calculations, and ARPES data we obtain new insights regarding the nature of the 2H-TaS_2 CDW phase transition. We identify the presence of three CDW modes below T_{CDW}, one zone-folded and two amplitude modes. The temperature- dependence of the amplitude modes deviate from the expectations of mean-field theory owing to quantum fluctuations but are captured by finite-temperature DFT calculations. Above T_{CDW}, we observe a strong two-phonon mode that originates from finite momentum phonons near the CDW wavevector. The energy of this feature is highly dependent upon temperature, suggesting that structural instabilities may exist on short length scales at temperatures T ~ 280 K. These Raman observations correlate with the CDW gap[2,24] closing temperature (T^*~240 K), estimated from the ARPES data as a function of temperature through T_{CDW}. Temperature-dependent DFT-calculations of the phonon band structure also indicate the appearance of a lattice instability at 280 K which further validates our interpretation. These results shed new light on layered CDW systems and provide the first correlated experimental-theoretical study of the 2H-TaS_2 system. We anticipate this work will spur further investigations

into the intriguing features of CDW phase transitions in various TMDs and find relevance in future efforts to incorporate CDW materials in non-volatile memory technology.[25–28]

Methods

2H-TaS_2 single crystals were grown by chemical vapor transport (CVT) using iodine as the transport gas. Energy-dispersive X-ray spectroscopy (EDX) scans reveal 66 ± 2 % Sulphur to Tantalum composition confirming their 2:1 stoichiometric ratio. Bulk flakes were mechanically exfoliated from these crystals using a low-tack blue semiconductor tape and transferred onto a Si/SiO_2 substrate (285 nm oxide) in air within 1 hour. These bulk samples were subsequently capped with h-BN to prevent any further degradation of the sample overtime. High-resolution, polarized Raman measurements were performed from 4 K - 90 K in a back-scattering configuration. The excitation laser was at 476 nm and was focused through a 50 × objective with 0.82 NA to achieve a 300 nm spot size on the sample. The laser power was ~ 100 μW before the objective. Scattered light was collected from the sample and directed towards a triple-grating spectrometer with a liquid-N_2 cooled Si-CCD detector. To perform polarization dependent measurements, we kept the excitation polarization constant and used a linear polarizer to select the parallel or cross polarization with a half wave plate to rotate the light to the polarization with higher efficiency in the triple grating spectrometer. All spectra are taken in the parallel polarization configuration unless otherwise specified. Raman spectra were taken at 4 K using 458 nm (2.7 eV), 476 nm (2.6 eV), 514 nm (2.41 eV), and 633 nm (1.95 eV) laser lines keeping the power, polarization, and setup constant. The high temperature Raman measurements (90 K-300 K) were carried out on a home-built confocal microscope setup with 532 nm laser excitation (2 μm spot size; ~1 mW laser power pre-objective), focused through a 0.5 NA, 50× long working distance objective. The light is collected in a back-scattering geometry, with the collection fiber-coupled to a 500 mm focal length single spectrometer integrated with a liquid-N_2 cooled CCD detector. The samples in both setups were kept under an inert environment between measurements.

The ARPES measurements were conducted using the 21.2 eV He I line of a discharge lamp combined with a Scienta R3000 analyzer at the University of Virginia. The angular resolution is ~0.3°, and the total energy resolution is ~8–10 meV. For temperature-dependent studies, ARPES data were collected in a cyclic way to ensure that there were no aging effects in the spectra. All experiments were performed in an ultrahigh vacuum (better than 5×10^{-11} Torr).

DFT calculations were carried out using the QUANTUM ESPRESSO (QE) package.[29] The exchange-correlation interaction was described by the local density approximations (LDA) using the Perdew-Wang parametrization of the correlation energy.[30] We used the norm-conserving pseudopotential[31] and the van der Waals density functional (vdW-DF) method to capture experimental non-local correlations.[32] This combination of exchange-correlation, pseudopotential and van der Waals correction was chosen as it gave an equilibrium lattice

constant in excellent agreement with available experimental data at room temperature (DFT: a = 0.338 nm, c = 1.220 nm, Exp: a = 0.334 nm, c = 1.217 nm).[33] The kinetic energy cutoff of the plane-wave expansion is taken as 50 Ry. All the geometric structures are fully relaxed until the force on each atom is less than 0.002 eV/Å, and the energy-convergence criterion is 1×10^{-6} eV. For the unit cell and supercell structure relaxation, we used a 16 × 16 × 16 and 3 × 3 × 8 k-point grid, respectively. Phonon calculations, we used a 4 × 4 × 4 uniform q-grid for unit cell and for the supercell we did only gamma point phonon calculation. While the DFT calculations were performed at 0 K, we modeled the temperature effects behind the formation of the CDW states by varying the electronic temperature, i.e. tuning the smearing factor σ, which describes the Fermi-Dirac distribution. This methodology has been introduced by Refs.[1,34–39] and allowed us to qualitatively assess the effect of temperature on the phonon properties of the system. To validate this approach, we computed the lattice parameters at different temperatures for the unit cell and compared it with available experimental results.[33] We found that our predicted lattice constant along the *c axis* is good agreement with experimental results. No experimental data are available for the dependence of lattice constant a on temperature. A 3 × 3 × 1 supercell was used to investigate the CDW structural transition, to allow for atomic rearrangement, if needed. As it has been experimentally shown that 2H-TaS_2 only CDW phase is incommensurate, we applied a perturbation along the c axis in the form of small compressive stress to computationally model incommensurability using a relatively small cell (3 × 3 × 1). This approach was first proposed by Janner *et al*.[40]

Results

Comparison of room temperature and low temperature Raman spectra reveal significant changes originating from the CDW transition. In Figure 1(b), we present 300 K Raman data for 2H-TaS_2 in the normal state (the state at temperatures above T_{CDW}) that was acquired with 532 nm excitation. Four prominent optical phonon modes are observed at 26 cm^{-1} (E_{2g}) 245 cm^{-1} (E_{1g}) 290 cm^{-1} (E_{2g}) and 404 cm^{-1} (A_{1g}) in agreement with prior studies.[21,22] The two-phonon feature at 180 cm^{-1} arises from second-order scattering of acoustic and quasi-acoustic modes near the CDW wavevector $q_{CDW} \cong \frac{2}{3}$ ΓM and is commonly observed in other Group V TMDs.[41,42–44] The data in Figure 1(b) can be fit (red curve) using a combination of eight Voigt functions. Two of these Voigt functions are used to account for the Rayleigh background and unassigned spectral weight in the 350 cm^{-1} spectral region. Raman mode symmetry is determined by polarization-resolved measurements and is in agreement with prior studies on 2H-TaS_2.[13,22,23,45] E and A symmetry modes are shaded in purple and gold, respectively. DFT calculations of the Raman data using the standard 2H-TaS_2 supercell structure reproduce mode frequencies within 15 cm^{-1} of experimental data and faithfully reproduce the mode symmetries.

The Raman spectra of 2H-TaS_2 is substantially modified when cooled below T_{CDW}. In Figure 1(c) we present 4 K Raman spectra in the CDW state taken with four different excitation wavelengths. These measurements were performed using a different cryostat that provides access

to multiple laser lines used for resonance Raman studies: 458 nm (2.7 eV), 476 nm (2.6 eV), 514 nm (2.14 eV) and 633 nm (1.95 eV). The spectra in Figure 1(c) are normalized by the intensity of the $^1A_{1g}$ mode at 404 cm^{-1} to ease comparison. The most obvious change in the data is the appearance of new sharp modes at 48 cm^{-1} (E_{amp}) and 78 cm^{-1} (A_{amp}) in all spectra as well as a weak feature at ~100 cm^{-1} that appears when exciting with 476 nm and 514 nm light. Polarization-dependent measurements of the 48 cm^{-1} and 78 cm^{-1} modes are included in the inset of Figure 1(c) and indicate the modes are of *E* and *A* symmetry. These new features at low wavenumber are clearly associated with the CDW state and are consistent with observations in Group V TMDs.[46–48] and are usually referred to as amplitude modes since they modulate the magnitude of the CDW rather than its phase.[22,45,23] Lack of inversion symmetry breaking in the incommensurate CDW state of bulk 2H-TaS_2 prevents the observation of phase modes by Raman scattering. The 100 cm^{-1} mode is too weak to be clearly resolved in polarization-dependent data, but likely emerges from zone-folding due to reconstruction of the BZ in the CDW state. DFT calculations predict the CDW modes and their symmetries, along with their atomic displacements shown in the top left corner (Figure 1(a)).

The optical modes observed at 300 K remain at 4 K with only small wavenumber shifts but with significant changes in intensity. The shear mode at 26 cm^{-1} (E_{2g}), two-phonon mode, and all modes between 180 cm^{-1} and 350 cm^{-1} are weakened relative to the mode at 404 cm^{-1} (A_{1g}) regardless of excitation wavelength. Amplitudons in 2H-TaS_2 appear to have an interesting dependence on excitation wavelength. In Figure 1(c), we observe that the relative intensity of the two most prominent CDW modes is roughly the same when excited with 458 nm light. Upon changing wavelength to 476 nm and 514 nm it is the E amplitude mode that dominates, a trend that reverses when using 633 nm excitation. Note that the weak 100 cm^{-1} zone-folded mode also appears in the 514 nm and 476 nm spectra, which when considered in concert with our DFT predictions clearly indicates that it does not arise from laser plasma lines or other spectral artifacts. The origin of these responses is unclear at present since there are no predicted optical transitions in this energy range to which the laser may be quasi-resonant. However, the data shown do provide guidance for us in terms of the optimal laser wavelengths to utilize in our studies.

A key signature of CDW amplitude modes is their softening and broadening when warming across T_{CDW}. We perform temperature-dependent Raman measurements in the range of 4 K to 90 K using 476 nm laser excitation (Figure 2(a)) to monitor changes of the modes relevant to the CDW instability. Figure 2(a) shows evolution of Raman spectra acquired at different temperatures in and out of the CDW phase with a sample fit shown for the scan taken at 4 K. The shaded gray hatched areas are fits to the Rayleigh background while the E (A) symmetry modes are in purple (gold). The weak 100 cm^{-1} zone-folded mode is also shown (in bright green), the fact that it stays static all the way across the CDW phase only to disappear at $T > T_{CDW}$ further validates our assignment that it originates from zone-folding mechanisms. The hallmark softening of CDW amplitude modes is clearly observed as the sample temperature is raised with

both modes red-shifting and broadening, finally becoming unresolvable at T > 70 K (Figure 2(a), 2(b) and 2(c)). We will elaborate upon the power-law scaling of these modes in the discussion section.

In Figure 3(a) we focus on a less commonly examined behavior in Group V TMD materials: the two-phonon mode. This Raman feature is associated with the strong wavevector-dependent electron-phonon coupling near the CDW wavevector. The two-phonon mode represents a second order process where phonon-assisted scattering of the electrons near the Fermi level leads to the creation of two phonons with equal and opposite wavevectors (i.e. $\overrightarrow{q_1} + \overrightarrow{q_2} = 0$).[42] All phonons that satisfy this condition collectively contribute to the two-phonon mode leading to its large width. Usually multi-phonon Raman processes are weaker than their one phonon counterparts, yet in TMDs with CDW transitions such modes tend to be rather strong.[49] The reason being that the Raman scattering amplitudes for this anomalous feature contains a term proportional to the magnitude of the associated electron-phonon coupling constant, which in materials that exhibit CDW and SC phase transitions, is much more dominant.[42] While driving the CDW transition, the ability of the electrons to screen phonons increases, which develops a sharper and deeper Kohn anomaly, but broader and weaker two-phonon mode. Therefore, monitoring the shift of this mode with temperature provides an indirect measure of the phonon branch renormalization, owing to the onset of the CDW phase.

With regards to the remaining optical modes identified in Figure 1(a), the behavior across T_{CDW} is less dramatic. The out-of-plane (A_{1g}) high-wavenumber mode at 404 cm^{-1} remains prominent upon cooling (Figure 3(a)) and survives to 4 K at which point it has slightly blue-shifted and sharpened. Other in-plane modes at 245 cm^{-1} (E_{1g}) and 290 cm^{-1} (E_{2g}) show insignificant shifts (Supplemental Figure S1)[50], however, the 290 cm^{-1} (E_{2g}) mode weakens in concert with the two-phonon mode despite being a Γ-point mode. The interlayer shear-mode at 26 cm^{-1} (E_{2g}) in Figure 1(b) remains prominent with decreasing temperature, indicating that the formation of a largely 2D CDW mode [51,52] that eventually is overshadowed by the CDW amplitude modes. The sharpening of the 404 cm^{-1} (A_{1g}) mode upon cooling to low temperature (Figure 3(c)) appears to display the same trend as the frequency of the two-phonon mode which suggests a common origin behind its anharmonicity.

Finally, we analyze temperature-dependent ARPES data from 2H-TaS_2 in Figure 4. To this end, we first focus on energy distribution curves (EDCs) in Figure 4(a), where an EDC is ARPES intensity as a function of energy at a specific momentum location[53]. These EDCs have been divided by the resolution-broadened Fermi function to approximately deconvolute the effects of energy resolution and Fermi function. Note that the same data set has been used in separate studies by our team in Ref. 24. The inset of Figure 4(b) shows the momentum location of the Fermi function divided EDCs in Figure 4(a). It is to be noted that the electronic energy in Figure 4(a) is referenced with respect to the chemical potential (μ) of the system. The Fermi function divided EDC at the lowest temperature shows that its peak closest to μ is actually located at a

negative energy indicating the presence of an energy gap due to CDW instability. In the present case, the exact magnitude of energy gap, however, can't be determined from the ARPES data. This is because the minimum of the Fermi function divided EDC at each temperature is located at a positive energy, which can't be detected unambiguously by ARPES. Such particle-hole asymmetry in energy gap is anticipated for a CDW system like 2H-TaS_2, where the CDW wave vector is not directly connected to Fermi surface nesting. Nevertheless, the presence or absence of an energy gap from ARPES data can be ascertained.

Discussion

The CDW amplitude modes are linked to the CDW complex order parameter and therefore are expected to exhibit mean-field like temperature dependence,[44]

$$\omega_{CDW}^{i}(T) \propto \sqrt{1 - \frac{T}{T_{CDW}}}, \tag{1}$$

where $\omega_{CDW}^{i}(T)$ is the temperature-depdendent mode frequency for amplitude mode. We display the temperature-dependent amplitude mode frequencies for the E and A symmetry amplitude modes in Figure 2(b) and 2(c) to illustrate that in 2H-TaS_2 this expectation fails dramatically. Mode softening is apparently incomplete, with both amplitude modes retaining non-zero frequencies immediately before the phase transition. This behavior is frequently observed in CDW materials and is frequently attributed to short-range fluctuations out of phase with local CDW order as in the case of 2H-$NbSe_2$,[54] $TiSe_2$,[55,56] and other CDW materials.[57–59] The pink dashed curve in each figure is a model fit to the expected mean-field dependence, which clearly cannot capture the observed temperature-dependence. If we instead relax the fitting function to have a varying power β and varying coefficient

$$\omega_{CDW}^{i}(T) = A\,\omega_{o}^{i}\left(1 - \frac{T}{T_{CDW}}\right)^{\beta}, \tag{2}$$

we find that an excellent fit can be obtained that provides reasonable values for T_{CDW} but unreasonable values for $\beta \approx 0.05$. The departure from square-root-dependence of CDW phonon softening has been observed in other CDW systems such as $TiSe_2$,[55,56] K_2SeO_4,[60] $A_{0.3}MoO_3$ (A = K, Rb)[61] and numerous rare-earth tritelluride compounds[57–59] with values of β ranging from 0.08 to 0.3. A very recent study of amplitude modes in 2H-TaS_2 observes this deviation as well, but fits their data using a modified mean-field fit.[23]

While a mean field theory approach is unable to capture the temperature dependence of CDW modes E_{amp} and A_{amp}, finite-temperature DFT is successful at it. Figures 5(a) and 5(b) compare DFT and experimental data for the change in frequency of E_{amp} and A_{amp} CDW modes as temperature increases. The scale in the figure is much tighter than in Figures 2(b) and 2(c). The experimental trend is well reproduced for both modes, and an amazing quantitative match is

found for A_{amp}. Such excellent agreement supports the modeling strategy we implemented to simulate the incommensurate CDW. It also validates the atomic structure we determined to be the equilibrium configuration in CDW phase. Comparing Figures 5(c) and 5(d), it is apparent that in-plane movement of Ta-atoms is behind the formation of the CDW phase. This Ta-atoms displacement was observed experimentally.[62] The final structure displays a triangular superlattice, much like what has been seen for 2H-$NbSe_2$.[63] Lastly, we note that our DFT calculations and experimental data disagree markedly with recent results where the authors claim to observe many more of CDW modes than we do and assign them as zone-folded phonons.[23]

The temperature-dependence of the two-phonon mode at $T > T_{CDW}$ is another curious behavior. We begin with the normal phase where the dominant two-phonon feature at 180 cm^{-1} in the 300 K spectrum softens and broadens with decreasing temperature in conjunction with the broadening of the in-plane E_{2g} mode at 290 cm^{-1} (Figure 3(a)). Second-order scattering processes such as this have contributions form an ensemble of phonons belonging to multiple acoustic branches, with equal and opposite momentum that traces the CDW wavevector q_{CDW}. The softening of the two-phonon feature then from 180 cm^{-1} at 300 K to 150 cm^{-1} at 90 K shown in Figure 3(b) (green points) is a response to the renormalization of the phonon frequencies approaching the phase transition temperature and a sign that the instability in the lattice is present at temperatures much higher than T_{CDW}. Interestingly, we also find that the linewidth of the dominant 404 cm^{-1} mode (Figure 3(c)) follows the same functional form as the two-phonon mode, suggesting that phonon-lifetime of the A_{1g} optical mode might be correlated with structural instability and presence of pseudo-gap indicated by the two-phonon feature. We note that defects provide one mechanism for stabilizing CDW above the critical temperature as has been shown in scanning tunneling microscopy measurements of $NbSe_2$.[64]

We find that the high-temperature shift of the two-phonon mode correlates with changes in the ARPES data above T_{CDW}. This is illustrated by Figure 4. A closer look at Figure 4(a) highlights that with increasing temperature, the strength of the peaks of the Fermi function divided EDCs get weaker, but the energy locations of the peaks are essentially the same. Even though the spectra at temperatures above T_{CDW} do not possess well-defined peaks, a clear signature of the suppression of low energy spectral weight is always present. This implies the CDW energy gap persists even in the normal state, i.e., for temperatures above T_{CDW}. The survival of CDW energy gap even at $\sim 100K\ (> T_{CDW})$, evidences a non-BCS like phase transition at T_{CDW}. This is consistent with the observations in Figures 2 and 3. The persistent energy gap above the transition temperature closely resembles the enigmatic pseudo-gap phase in underdoped cuprate high temperature superconductors (HTSC).[65] It is then natural to speculate that similar to the pseudo-gap closing temperature in cuprate HTSCs, there would be a temperature T^* a 2H-TaS_2 at which the normal state CDW energy gap disappears. We obtain an approximate value of T^* by conducting an analysis of the filling up of the energy gap via an accumulation of spectral weight at zero energy (ω) as a function of T. We plot $L(T) = 1 - \frac{I(T,\omega=0)}{I(T,\omega=\omega_{peak})}$ for different values of T

in Figure 4(b), where at a given temperature T, $I(T, \omega = 0)$ is the intensity of the Fermi function divided data at $\omega = 0$ and $I(T, \omega = \omega_{peak})$ is the intensity at $\omega = \omega_{peak}$ with ω_{peak} being the energy location of the peak or kink-like structure of the Fermi function divided EDC. Thus, from the extrapolation of $L(T)$ to zero, T^* can be estimated. Figure 4(b) shows that the estimated value of T^* in the current case is $\sim 240K$, which is substantially higher than $T_{CDW} \sim 75K$. Similar analysis has been extensively used in cuprate HTSCs to determine pseudo-gap temperature[66,67] as well as in $ZrTe_3$.[59] It should be noted that such a large value of T^* is not unprecedented in 2H polytypes of the TMDs—for instance, ARPES studies on 2H-$NbSe_2$ suggest CDW order close to room temperatures[68] even though its $T_{CDW} \sim 33K$. The fact that there is a temperature range in which the structural instability, manifested by softening of the two-phonon mode, coexists with an energy gap above T_{CDW}, suggests that they are connected. This reiterates the significance of electron-phonon coupling in the CDW instability of 2H-TaS_2 and that of incommensurate transition metal dichalcogenides (TMDs), in general.

To better understand how temperature affects the vibrational modes of 2H-TaS_2 and at what temperature the first signs of structural instability appear, we calculated the phonon band structure at different temperatures across the CDW transition. The phonon band structures are calculated with the standard 2H-TaS_2 unit cell (6 atoms, 18 bands), instead of our usual 3 × 3 × 1 supercell. While this enabled us to clearly follow the changes of each band it does not allow for a direct modeling of the incommensurate CDW phase as the cell is too small to allow atomic rearrangement. Therefore, we apply the same compressive strain along the *c*-axis and Fermi surface smearing used in the prior super-cell simulations. We computed the phonon band structure using several k-points meshes (8 × 8 × 8, 12 × 12 × 12, 16 × 16 × 16 and 24 × 24 × 24), to guarantee convergence, and present results obtained using 24 × 24 × 24 k-point mesh. The complete picture of the phonon band structure of 2H-TaS_2 at six different temperatures (T = 300 K , 280 K, 250 K, 150 K, 70 K and 30 K) is presented in Figure 6. The three acoustic (red curves) and three quasi-acoustic bands (blue curves) shown in Figure 6(a) and 6(b) respectively are separated from the optical bands (Figure 6(c), black curves) by a large (75 cm^{-1}) indirect phonon frequency gap. Approaching the CDW transition temperature, while the optical bands exhibit essentially no temperature dependence close to T_{CDW} (Figure 6(c)), the story is quite different for the acoustic and quasi acoustic modes. Our calculations of the full acoustic phonon dispersion at different temperatures, indicates that the phonon frequencies remain positive until 280 K. For all temperatures at or below 250 K we observe signs of a lattice instability as negative phonon frequencies appear in the acoustic branches along the ΓM direction. Below 100 K, the same acoustic branches become negative along the ΓK direction as well. The quasi-acoustic branches show a very similar temperature dependence as presented in Figure 6(b). However, we find a curious behavior near the K point where the quasi-acoustic branches increase in energy while the acoustic branches decrease and become negative with decreasing temperature. While investigating unit cell vibrational modes does not allow for the qualitative estimate of the temperature at which the incommensurate CDW phase forms (T_{CDW}), it reveals

that structural instabilities start at temperatures much higher than the expected T_{CDW}. This is, again, in good agreement with our experimental findings.

Finally, to understand the evolution of the two-phonon mode with temperature, we compare the DFT predictions for both UC and 3 × 3 × 1 supercell to the experimental results (Supplemental Figure S2)[50]. UC calculations allow us to identify location of the Kohn anomaly, which is found between the Γ and M points, but are limited by the fact that the tiny cell doesn't permit significant atomic rearrangement. An excellent agreement is found between the 3 × 3 × 1 DFT results and the experimental ones, while the UC DFT findings show the correct trend but predicts a red shift three times larger than the one obtained for the 3 × 3 × 1 supercell. One advantage of DFT modeling is that it gives access to the actual vibrations related to each identified mode, and the atomic vibration corresponding to the two-phonon mode are shown in Supplemental Figure S2.[50]

Conclusion

In summary, we have carried out the first correlated experimental-theoretical study of CDWs in 2H-TaS_2. These observations confirm the presence of two amplitude modes and a zone-folded mode below T_{CDW} that exhibit an anomalous temperature dependence. DFT successfully capture this behavior and provide a physical picture regarding the atomic displacements arising from amplitudons. Analysis of the two-phonon mode is correlated with ARPES and DFT data to suggest the presence of short-range CDW order even well above the phase transition temperature. These results show that CDWs in layered systems are more complicated than previously thought and that CDW physics is relevant even at temperatures well-above T_{CDW}.

Acknowledgements

We gratefully acknowledge assistance from Albert D. Davydov in energy dispersive x-ray scattering measurements and useful discussions with T.M. Vora. P.M.V and J.J. acknowledge support from the National Science Foundation under Grant No. DMR-1748650 and the George Mason University Quantum Materials Center. U. C. acknowledges supports from the National Science Foundation under Grant No. DMR-1454304 and the Jefferson Trust at the University of Virginia. H.M.H. would like to thank the National Research Council's Research Associateship Program.

Reference

[1] F. Weber, S. Rosenkranz, J.P. Castellan, R. Osborn, R. Hott, R. Heid, K.P. Bohnen, T. Egami, A.H. Said, and D. Reznik, Phys. Rev. Lett. **107**, 6 (2011).
[2] K. Wijayaratne, J. Zhao, C. Malliakas, D. Young Chung, M.G. Kanatzidis, and U. Chatterjee, J. Mater. Chem. C **5**, 11310 (2017).
[3] L.P. Gor'kov, Phys. Rev. B **85**, 165142 (2012).
[4] X. Zhu, J. Guo, J. Zhang, and E.W. Plummer, Adv. Phys. X **2**, 622 (2017).
[5] D.S. Inosov, V.B. Zabolotnyy, D. V. Evtushinsky, A.A. Kordyuk, B. Büchner, R. Follath, H.

Berger, and S. V. Borisenko, New J. Phys. **10**, (2008).
[6] M. Johannes, I. Mazin, and C. Howells, Phys. Rev. B **73**, 205102 (2006).
[7] J. van Wezel, P. Nahai-Williamson, and S.S. Saxena, Phys. Rev. B **81**, 165109 (2010).
[8] J. van Wezel, P. Nahai-Williamson, and S.S. Saxena, Phys. Rev. B **83**, 024502 (2011).
[9] C. Monney, C. Battaglia, H. Cercellier, P. Aebi, and H. Beck, Phys. Rev. Lett. **106**, 106404 (2011).
[10] K. Rossnagel, J. Phys. Condens. Matter **23**, 213001 (2011).
[11] X. Xi, Z. Wang, W. Zhao, J.H. Park, K.T. Law, H. Berger, L. Forró, J. Shan, and K.F. Mak, Nat. Phys. **12**, 139 (2016).
[12] Y. Yang, S. Fang, V. Fatemi, J. Ruhman, E. Navarro-Moratalla, K. Watanabe, T. Taniguchi, E. Kaxiras, and P. Jarillo-Herrero, Phys. Rev. B **98**, 035203 (2018).
[13] E. Navarro-Moratalla, J.O. Island, S. Mañas-Valero, E. Pinilla-Cienfuegos, A. Castellanos-Gomez, J. Quereda, G. Rubio-Bollinger, L. Chirolli, J.A. Silva-Guillén, N. Agraït, G.A. Steele, F. Guinea, H.S.J. van der Zant, and E. Coronado, Nat. Commun. **7**, 11043 (2016).
[14] S.C. de la Barrera, M.R. Sinko, D.P. Gopalan, N. Sivadas, K.L. Seyler, K. Watanabe, T. Taniguchi, A.W. Tsen, X. Xu, D. Xiao, and B.M. Hunt, Nat. Commun. **9**, 1427 (2018).
[15] S. Sugai, Phys. Status Solidi **129**, 13 (1985).
[16] M. Yoshida, J. Ye, Y. Zhang, Y. Imai, S. Kimura, A. Fujiwara, T. Nishizaki, N. Kobayashi, M. Nakano, and Y. Iwasa, Nano Lett. **17**, 5567 (2017).
[17] R.A. Craven and S.F. Meyer, Phys. Rev. B **16**, 4583 (1977).
[18] R.V. Coleman, W.W. McNairy, C.G. Slough, P.K. Hansma, and B. Drake, Surf. Sci. **181**, 112 (1987).
[19] W.Z. Hu, G. Li, J. Yan, H.H. Wen, G. Wu, X.H. Chen, and N.L. Wang, Phys. Rev. B **76**, 045103 (2007).
[20] L. Li, X. Deng, Z. Wang, Y. Liu, M. Abeykoon, E. Dooryhee, A. Tomic, Y. Huang, J.B. Warren, E.S. Bozin, S.J.L. Billinge, Y. Sun, Y. Zhu, G. Kotliar, and C. Petrovic, Npj Quantum Mater. **2**, 11 (2017).
[21] R. Zhao, B. Grisafe, R.K. Ghosh, S. Holoviak, B. Wang, K. Wang, N. Briggs, A. Haque, S. Datta, and J. Robinson, 2D Mater. **5**, 025001 (2018).
[22] S. Sugai, K. Murase, S. Uchida, and S. Tanaka, Solid State Commun. **40**, 399 (1981).
[23] R. Grasset, Y. Gallais, A. Sacuto, M. Cazayous, S. Mañas-Valero, E. Coronado, and M.-A. Méasson, ArXiv **1806.03433** (2018).
[24] J. Zhao, K. Wijayaratne, A. Butler, J. Yang, C.D. Malliakas, D.Y. Chung, D. Louca, M.G. Kanatzidis, J. van Wezel, and U. Chatterjee, Phys. Rev. B **96**, 125103 (2017).
[25] M. Yoshida, R. Suzuki, Y. Zhang, M. Nakano, and Y. Iwasa, Sci. Adv. **1**, e1500606 (2015).
[26] A. Khitun, G. Liu, and A.A. Balandin, IEEE Trans. Nanotechnol. **16**, 860 (2017).
[27] G. Liu, E.X. Zhang, C.D. Liang, M.A. Bloodgood, T.T. Salguero, D.M. Fleetwood, and A.A. Balandin, IEEE Electron Device Lett. **38**, 1724 (2017).
[28] M. Hossain, Z. Zhao, W. Wen, X. Wang, J. Wu, and L. Xie, Crystals **7**, 298 (2017).
[29] P. Giannozzi, S. Baroni, N. Bonini, M. Calandra, R. Car, C. Cavazzoni, D. Ceresoli, G.L. Chiarotti, M. Cococcioni, I. Dabo, A. Dal Corso, S. de Gironcoli, S. Fabris, G. Fratesi, R. Gebauer, U. Gerstmann, C. Gougoussis, A. Kokalj, M. Lazzeri, L. Martin-Samos, N. Marzari, F. Mauri, R. Mazzarello, S. Paolini, A. Pasquarello, L. Paulatto, C. Sbraccia, S. Scandolo, G. Sclauzero, A.P. Seitsonen, A. Smogunov, P. Umari, and R.M. Wentzcovitch, J. Phys. Condens. Matter **21**, 395502 (2009).
[30] J.P. Perdew and Y. Wang, Phys. Rev. B **45**, 13244 (1992).

[31] D. Vanderbilt, Phys. Rev. B **41**, 7892 (1990).
[32] K. Berland, C.A. Arter, V.R. Cooper, K. Lee, B.I. Lundqvist, E. Schröder, T. Thonhauser, and P. Hyldgaard, J. Chem. Phys. **140**, 18A539 (2014).
[33] F.L. Givens and G.E. Fredericks, J. Phys. Chem. Solids **38**, 1363 (1977).
[34] M. Calandra, I.I. Mazin, and F. Mauri, Phys. Rev. B **80**, 241108 (2009).
[35] D.L. Duong, M. Burghard, and J.C. Schön, Phys. Rev. B **92**, 245131 (2015).
[36] J.-A. Yan, M.A. Dela Cruz, B. Cook, and K. Varga, Sci. Rep. **5**, 16646 (2015).
[37] G. Grüner, *Density Waves in Solids* (CRC Press, 1994).
[38] K. Motizuki, N. Suzuki, Y. Yoshida, and Y. Takaoka, Solid State Commun. **40**, 995 (1981).
[39] N.D. Mermin, Phys. Rev. **137**, 1 (1965).
[40] A. Janner, T. Janssen, and P.M. de Wolff, Europhys. News **13**, 1 (1982).
[41] X. Xi, L. Zhao, Z. Wang, H. Berger, L. Forró, J. Shan, and K.F. Mak, Nat. Nanotechnol. **10**, 765 (2015).
[42] M. V. Klein, Phys. Rev. B **24**, 4208 (1981).
[43] P. Hajiyev, C. Cong, C. Qiu, and T. Yu, Sci. Rep. **3**, 2593 (2013).
[44] J.C. Tsang, J.E. Smith, and M.W. Shafer, Phys. Rev. Lett. **37**, 1407 (1976).
[45] W.G. McMullan and J.C. Irwin, Can. J. Phys. **62**, 789 (1984).
[46] O.R. Albertini, R. Zhao, R.L. McCann, S. Feng, M. Terrones, J.K. Freericks, J.A. Robinson, and A.Y. Liu, Phys. Rev. B **93**, 214109 (2016).
[47] R. Samnakay, D. Wickramaratne, T.R. Pope, R.K. Lake, T.T. Salguero, and A.A. Balandin, Nano Lett. **15**, 2965 (2015).
[48] S.S. Jaswal, Phys. Rev. B **20**, 5297 (1979).
[49] M. Hangyo, S.-I. Nakashima, and A. Mitsuishi, Ferroelectrics **52**, 151 (1983).
[50]See Supplementary Material at "Insert Link Here" for more details on the temperature-dependence of other optical modes and DFT calculations of the two-phonon feature.
[51] A.A. Puretzky, L. Liang, X. Li, K. Xiao, B.G. Sumpter, V. Meunier, and D.B. Geohegan, ACS Nano **10**, 2736 (2016).
[52] C.H. Lui, Z. Ye, C. Ji, K.-C. Chiu, C.-T. Chou, T.I. Andersen, C. Means-Shively, H. Anderson, J.-M. Wu, T. Kidd, Y.-H. Lee, and R. He, Phys. Rev. B **91**, 165403 (2015).
[53] S. Hüfner, *Photoelectron Spectroscopy* (Springer Berlin Heidelberg, Berlin, Heidelberg, 2003).
[54] U. Chatterjee, J. Zhao, M. Iavarone, R. Di Capua, J.P. Castellan, G. Karapetrov, C.D. Malliakas, M.G. Kanatzidis, H. Claus, J.P.C. Ruff, F. Weber, J. van Wezel, J.C. Campuzano, R. Osborn, M. Randeria, N. Trivedi, M.R. Norman, and S. Rosenkranz, Nat. Commun. **6**, 6313 (2015).
[55] L. Cui, R. He, G. Li, Y. Zhang, Y. You, and M. Huang, Solid State Commun. **266**, 21 (2017).
[56] H. Barath, M. Kim, J.F. Karpus, S.L. Cooper, P. Abbamonte, E. Fradkin, E. Morosan, and R.J. Cava, Phys. Rev. Lett. **100**, 2 (2008).
[57] H.-M. Eiter, M. Lavagnini, R. Hackl, E.A. Nowadnick, A.F. Kemper, T.P. Devereaux, J.-H. Chu, J.G. Analytis, I.R. Fisher, and L. Degiorgi, Proc. Natl. Acad. Sci. **110**, 64 (2013).
[58] M. Maschek, S. Rosenkranz, R. Heid, A.H. Said, P. Giraldo-Gallo, I.R. Fisher, and F. Weber, Phys. Rev. B **91**, 235146 (2015).
[59] Y. Hu, F. Zheng, X. Ren, J. Feng, and Y. Li, Phys. Rev. B **91**, 144502 (2015).
[60] W.K. Lee, H.Z. Cummins, R.M. Pick, and C. Dreyfus, Phys. Rev. B **37**, 6442 (1988).
[61] D.M. Sagar, D. Fausti, S. Yue, C.A. Kuntscher, S. van Smaalen, and P.H.M. van Loosdrecht, New J. Phys. **10**, 023043 (2008).

[62] J. Dai, E. Calleja, J. Alldredge, X. Zhu, L. Li, W. Lu, Y. Sun, T. Wolf, H. Berger, and K. McElroy, Phys. Rev. B **89**, 165140 (2014).
[63] C.D. Malliakas and M.G. Kanatzidis, J. Am. Chem. Soc. **135**, 1719 (2013).
[64] C.J. Arguello, S.P. Chockalingam, E.P. Rosenthal, L. Zhao, C. Gutiérrez, J.H. Kang, W.C. Chung, R.M. Fernandes, S. Jia, A.J. Millis, R.J. Cava, and A.N. Pasupathy, Phys. Rev. B **89**, 235115 (2014).
[65] T. Timusk and B. Statt, Reports Prog. Phys. **62**, 61 (1999).
[66] U. Chatterjee, D. Ai, J. Zhao, S. Rosenkranz, A. Kaminski, H. Raffy, Z. Li, K. Kadowaki, M. Randeria, M.R. Norman, and J.C. Campuzano, Proc. Natl. Acad. Sci. **108**, 9346 (2011).
[67] A. Kanigel, M.R. Norman, M. Randeria, U. Chatterjee, S. Souma, A. Kaminski, H.M. Fretwell, S. Rosenkranz, M. Shi, T. Sato, T. Takahashi, Z.Z. Li, H. Raffy, K. Kadowaki, D. Hinks, L. Ozyuzer, and J.C. Campuzano, Nat. Phys. **2**, 447 (2006).
[68] S. V. Borisenko, A.A. Kordyuk, V.B. Zabolotnyy, D.S. Inosov, D. Evtushinsky, B. Büchner, A.N. Yaresko, A. Varykhalov, R. Follath, W. Eberhardt, L. Patthey, and H. Berger, Phys. Rev. Lett. **102**, 166402 (2009).

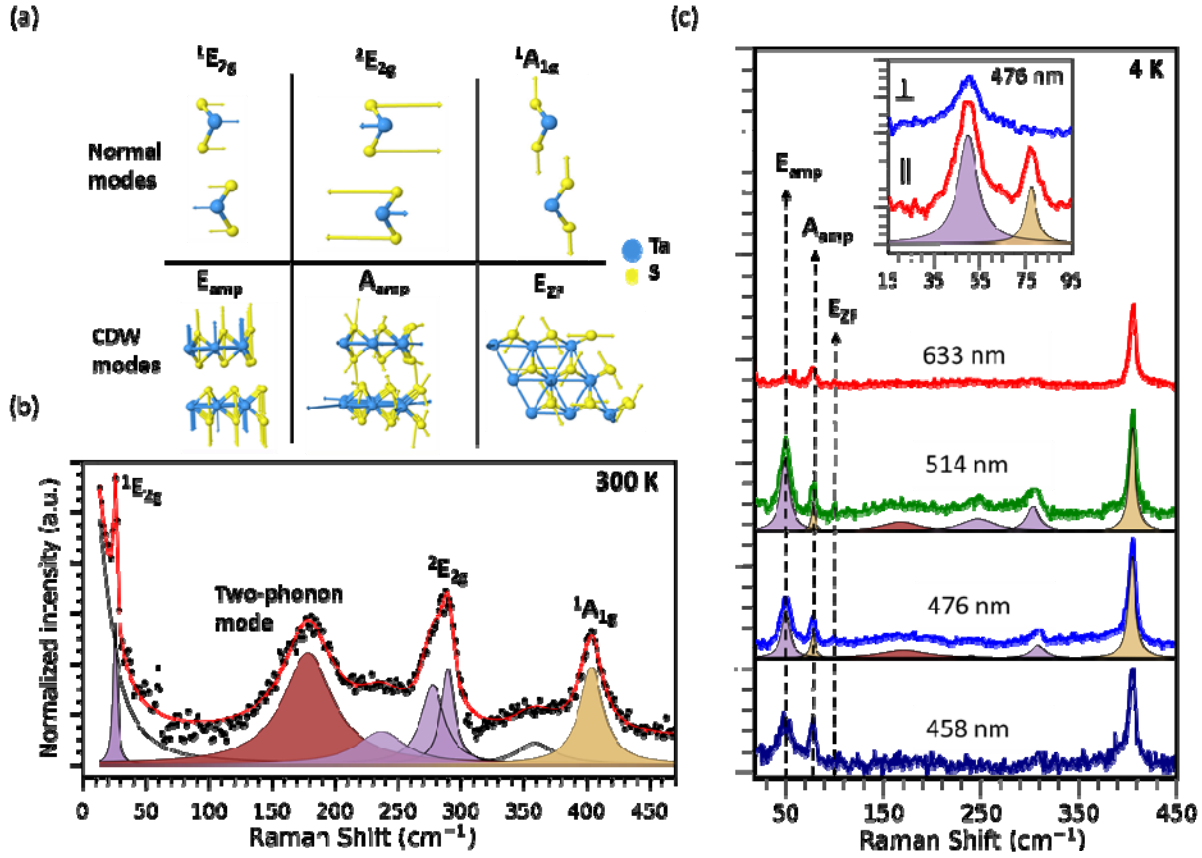

FIG. 1. (a) Mode displacement diagrams corresponding to modes in the normal and CDW phase are included next to the plots. **(b)** Room-temperature Raman spectra of bulk TaS_2 with observed modes and

their assignments. The two-phonon mode is shaded brown. Purple and golden shades represent modes with E and A symmetry respectively. Grey areas represent fits to the laser Rayleigh line and other features not predicted to be part of the material's Raman spectrum. Mode displacement for all one-phonon Raman scattering processes included as insets near each mode. (**c)** Excitation-dependent Raman measurements performed at 4 K with 458 nm (2.7 eV), 476 nm (2.6 eV), 514 nm (2.4 eV) and 633 nm (1.95 eV) laser wavelength. Peaks E_{amp}, A_{amp} correspond to CDW modes amplitude modes and E_{ZF} is the zone-folded CDW mode.

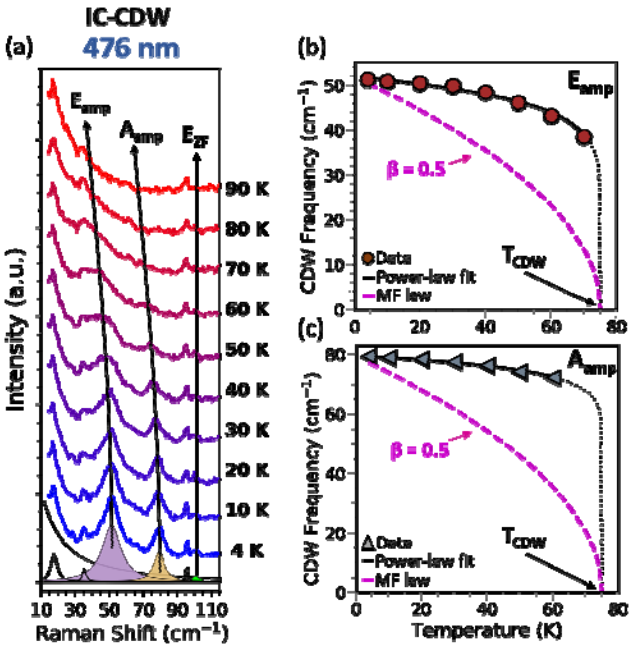

FIG. 2. (**a)** Temperature-dependent Raman measurements of the CDW modes E_{amp} and A_{amp} using 476 nm excitation with a sample Lorentzian fit shown for the data at 4 K. (**b**) Frequency of CDW mode E_{amp} extracted from the fits plotted as a function of temperatures. The value of is fixed at 75 K (**c)** Frequency of CDW mode A_{amp} extracted from the fits plotted as a function of temperature. The value of is fixed at 75 K. Dashed magenta line shows a model fit to mean-field theory equation with square-root dependence.

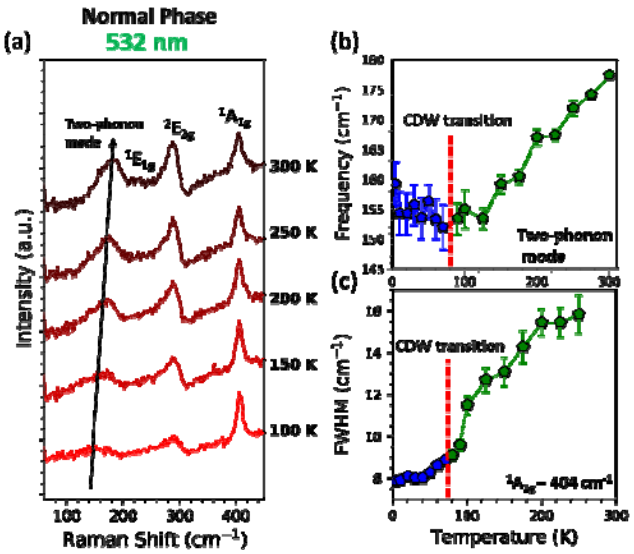

FIG. 3. (**a)** Temperature-dependent Raman measurements of the higher frequency modes in the metallic phase using 532 nm laser excitation. (**b**) Evolution of the two-phonon mode frequencies with temperature in and out of the CDW phase as a function of temperature. Below , the mode freezes in response to the CDW modulation while softens at higher temperatures. (**c)** FWHM of the high wavenumber optical mode at $^1A_{1g}$ 404 cm^{-1} showing similar broadening response at higher temperatures whereas the phonon linewidth remains pretty consisted inside the CDW regime.

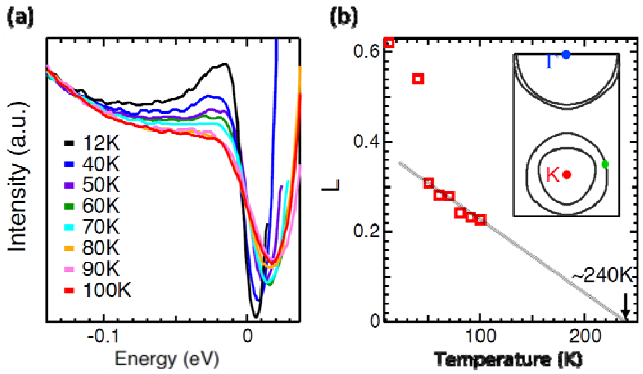

FIG. 4. (**a)** Fermi function divided EDCs with increasing temperature through T_{CDW}. **(b)** The green dot on the schematic plot of the Fermi surface in the inset shows the momentum location of the Fermi function divided EDCs in a. Temperature dependence of the spectral weight at the chemical potential. Extrapolation of ———— to zero provides an estimate of , which is much larger than T_{CDW}.

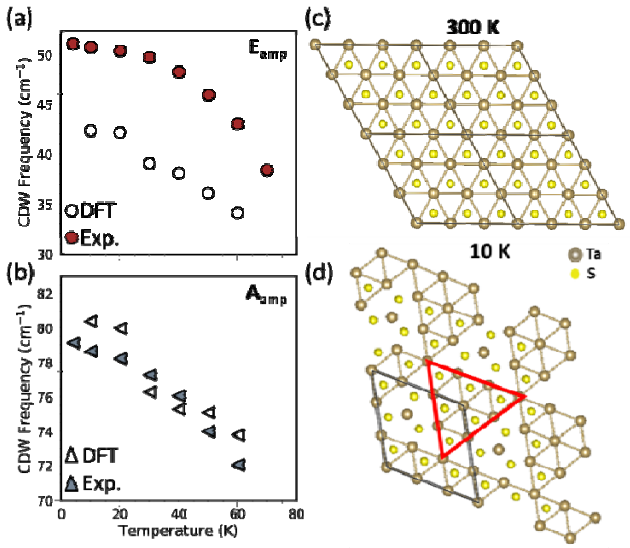

FIG. 5. **(a)** Frequency of the E_{amp} CDW modes at each temperature obtained using DFT and compared with experimental observations. **(b)** Frequency of the A_{amp} CDW modes at each temperature obtained using DFT and compared with experimental observations. **(c)** Lattice configuration of bulk 2H-TaS_2 at 300 K in the normal metallic phase. d. Evolution of a triangular configuration in the CDW regime.

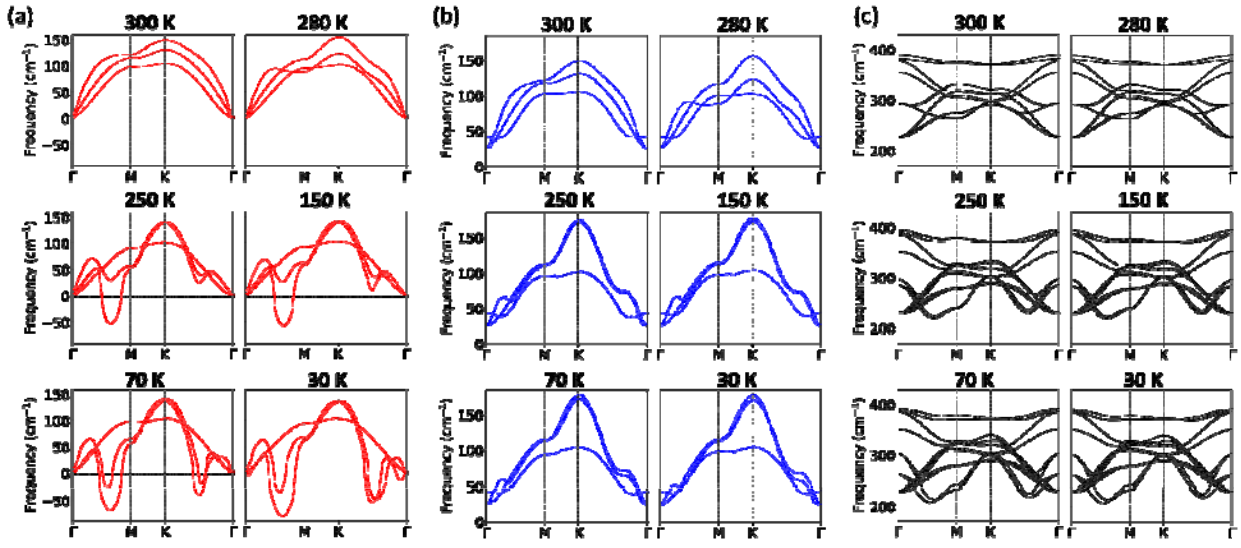

FIG. 6. DFT-calculated phonon dispersion curves for 2H-TaS_2. The **(a)** acoustic, **(b)** quasi-acoustic, and **(c)** optical modes are presented at temperatures in and out of the CDW phase (T = 300 K, 280 K, 250 K, 150 K, 100 K, 70 K and 30 K). The conventional unit cell is used for these calculations.